

PAPER



Cite this: *Dalton Trans.*, 2020, **49**, 13406

Correlation of dynamical disorder and oxy-ion diffusion mechanism in a Dy, W co-doped $\text{La}_2\text{Mo}_2\text{O}_9$ system: an electrolyte for IT-SOFCs†

Ruhi Naz Nayyar,^{a,b} Shyamkant Anwane,^b Vishwajit Gaikwad,^b Vasant Sathe^d and Smita Acharya^{*,a}

In the present attempt, a Dy, W co-doped $\text{La}_2\text{Mo}_2\text{O}_9$ (LMX) system is explored to understand the order-disorder phase transition, dynamical disorder state and their influence on the oxy-ion diffusion mechanism. The X-ray diffraction study confirms the co-dopant induced suppression of the order-disorder phase transition temperature of LMX. The oxygen ion diffusion in the LMX matrix is through intrinsic oxygen vacancies. Disorder oxygen vacancies enhance the degree of freedom of oxy-ion diffusion; these are related to the dynamical disorder states in LMX. These disorder states are demonstrated by high temperature Raman spectra. Dynamical disordering of oxygen vacancies in co-doped LMX systems is revealed by studying the rate of change of intensity of the Mo–O bond vibration as a function of temperature; non-uniformity in the rate of change of intensity is correlated to dynamical disorder. The dielectric relaxation studied by using dielectric loss spectra reveals a single relaxation peak for the pure-LMX system, while two dielectric relaxation peaks are revealed for doped LMX systems. Oxygen vacancy reorientation associated with dielectric relaxation is correlated to the diffusion process between O(1) → O(2) and O(1) → O(3) oxygen ion-vacancy exchange sites in doped LMX systems, while it is O(1) through orderly arranged oxygen vacancies in the pure LMX system. To ascertain the relaxation dynamics of the bulk system, electric modulus formalism is helpful, M'' data are fit by the Bergman function represented by the Kohlrausch–Williams–Watts (KWW) formula and non-Debye type relaxation is revealed for all systems. The activation energy of oxy-ion diffusion is reduced by a co-doping effect. Ionic conductivity extracted from complex impedance spectra indicates that oxy-ion conductivity in a co-doped LMX system is improved almost one order as compared to the pure system. The study reveals that a co-doped LMX system has the potential to be used as electrolytes for intermediate temperature solid oxide fuel cells (400–700 °C, IT-SOFCs).

Received 23rd August 2020,
Accepted 26th August 2020

DOI: 10.1039/d0dt02954h

rsc.li/dalton

1. Introduction

In recent years, creating new materials with the highest possible oxygen ion conductivity is a priority issue in the context of the development of advance power sources capable of chemical-to-electrical energy conversion. These materials are exten-

sively usable in electrochemical applications including solid oxide fuel cell, oxygen separation membrane and gas sensors. A novel complex oxide system lanthanum molybdate $\text{La}_2\text{Mo}_2\text{O}_9$ (LMX) has been first reported by Fournier *et al.*¹ and exploited by Lacorre *et al.*² as fast oxygen ion conductors. This material undergoes a structural phase transition from a monoclinic (α -phase) to a cubic (β phase) structure around 580 °C. At this transition temperature, oxide-ion conductivity has been found to be increased sharply by almost two orders of magnitude. The $\alpha \rightarrow \beta$ phase change is a transition in the distribution of the oxygen defects, from long-range order to short-range order. The long-range ordering of oxygen defects is referred to as a static disorder state, while short range ordering of oxygen vacancies is referred to as a dynamic disorder state. Like other traditional oxygen ionic conductors, the mechanism of ionic conduction in LMX also originates from the directional diffusion of oxygen ions *via* intrinsic oxygen vacancies in the

^aDepartment of Physics, Advanced Materials Research Laboratory, RTM Nagpur University, Nagpur 440033, India. E-mail: saha275@nagpuruniversity.nic.in

^bDepartment of Physics, Shri Shivaji Science College, Nagpur 440012, India

^cDepartment of Physics, Indian Institute of Technology Guwahati, Guwahati, Assam 781039, India

^dUGC-DAE-CSR, University Campus, Khandwa Road, Indore 452001, India

†Electronic supplementary information (ESI) available: Detail explanation on procedure of deconvolution of Raman spectra. Fig. S1-Deconvoluted data of Raman spectra at 550, 580 and 700 °C of LMX, LMXD-1, LMXD-2, LMXD-3. Fig. S2-Magnified view of High temperature Raman spectra of LMX. See DOI: 10.1039/D0DT02954H

crystal lattice. The high concentration of intrinsic O vacancies provides enough paths for O ion diffusion and is responsible for the high oxy-ion conductivity of LMX. Its conductivity at 800 °C is 0.08 S cm⁻¹,³ which is comparable to that of other oxy-ion conductors like doped perovskites,^{4,5} Zirconia based system⁶⁻⁸ pyrochlores,^{9,10} BIMEVOX¹¹⁻¹⁵ *etc.* These are extensively studied as high temperature oxy-ion conductors.

The conductivity of the LMX system is found to systematically fall with decreasing temperature, which is normal thermal activation behaviour. However, there is an abrupt reduction in conductivity by almost two orders of magnitude at the order-disorder phase transition ($T_c = 580$ °C). By tailoring the phase transition temperature of these groups of systems, low temperature oxy-ion conductivity can be achieved. Substitutions of both La and Mo sites have been examined in an attempt to further enhance the properties of lanthanum molybdate.¹⁶⁻²⁰ Studies on the substitution effect of lanthanum Ce³⁺, Y³⁺, Sm³⁺, Gd³⁺, Yb³⁺, Dy³⁺, Nd³⁺, Er³⁺ *etc.* on the La site have demonstrated the suppression of the $\alpha \rightarrow \beta$ phase transformation with enhancement in conductivity at the lower temperature side, *i.e.* below transition temperature (580 °C), except Nd³⁺. The Nd³⁺ substitution partially stabilizes the monoclinic distortion at room temperature, and the high temperature conductivity slightly improves with Nd³⁺ substitution. There is no significant enhancement in conductivity observed at a lower temperature (<580 °C).^{21,22} Amongst various substitutions, Er³⁺ and Dy³⁺ substitutions have been found to be the most effective rare earth substitutions.²³⁻²⁸ The alkaline element (Ca²⁺, Sr²⁺, Ba²⁺) doping effect in LMX leads to the formation of extrinsic oxygen vacancies. The suppression of phase transition and conductivity is found to strongly depend on the dopant content.²⁴⁻²⁶ Moreover, monovalent alkaline dopant K⁺ and Rb⁺ has also been observed to successfully suppress the phase transition. The monovalent cations give rise to extra oxygen vacancies, while the effect of increasing conductivity by extrinsic vacancies has not been found significant. There is a decrease in electrical conductivity by K⁺ and Rb⁺.^{27,28} The Mo sites' substitutional effect by V⁵⁺, W⁶⁺, and Cr⁶⁺ is mainly beneficial for reducing the reducibility of molybdenum in LMX.²⁹⁻³³ The redox-stability results show that W helps to avoid oxygen loss and decomposition under reduced conditions, while the total conductivity decreases. The Nb⁵⁺ substitution on the Mo sites has not been found to suppress phase transition, while improving the conductivity, which is almost double that of the parent materials.³⁴ Al³⁺ substitution on Mo sites has shown enhancement in the stabilization of LMX in a reduced atmosphere compared to tungsten.³⁵ Amongst various dopants on Mo-sites, V⁵⁺ doping has been reported to be suppressed by the phase transition whilst improving conductivity.³⁶ So, in the past few years, the substitutional effect in LMX for La or Mo sites has been proved to have the ability to improve performance compared to the parent materials; however many discrepancies are found in the results related to the effect of dopants on the suppression of phase transition and enhancement in ionic conductivity. Moreover, Subasri *et al.*³⁷ claimed that phase transition does

not have any direct influence on the total conductivity of the materials. There is hardly any strategic work to understand the role of dopants on the suppression of phase transition and enhancement of ionic conductivity in LMX systems. By considering the advantages and disadvantages of the substitution effect on La and Mo sites, double substitutions provide the opportunity to improve the stability of La₂Mo₂O₉ by suppressing the phase transition and improving ionic conductivity. As Er³⁺ and Dy³⁺ substitutions have been reported to be the most effective rare earth substitutions,²³ hexavalent tungsten, as the heaviest transition element, is reported to be more stable than hexavalent molybdenum.³⁸ So, a doubly substituted system of Dy³⁺ and W⁶⁺ is chosen to reveal their role on structure and ionic conductivity and thus modulation in the performance of the LMX system. A structural insight of the two (α and β) phases is important for better understanding the effect of site substitutions on the structure and oxygen diffusion mechanism through intrinsic oxygen vacancy defects in the system.

In the present study, we develop La_{1-x}Dy_xMo_{1-y}W_yO₉ to understand the multisite doping effect *i.e.* La and Mo sites by Dy and W, respectively, on order-disorder phase transition, dynamic disorder state and oxygen ion diffusion. As the multisite doping effect introduces lattice strain and changes the electrostatic interaction between cations and anions, it modifies the thermophysical properties of the parent system. A partial doping of W⁶⁺ at the Mo⁶⁺ site seems to be most suitable due to the high stability of W⁶⁺ under a reducing atmosphere, and the ionic radius of W⁶⁺ (0.60 Å) is similar to Mo⁶⁺ (0.59 Å), permitting high-level substitution. This study was restricted to compositions having a tungsten content $y = 0.3$. It has been observed that at a higher substitution concentration, the high temperature β -form is not thermodynamically stable in the air above 700 °C.³⁹ We optimized the Dy content to obtain a single phase of LMX. For sample preparation, a sol-gel synthesis route was used to get good chemical homogeneity. The effect of a co-dopant on the phase transition and dynamics of oxy-ion conductivity of the LMX system is revealed by using XRD, high temperature Raman spectroscopy, and dielectric and impedance spectroscopy studies.

2. Experimental procedure

Polycrystalline and single phase La_{2-x}Dy_xMo_{1.7}W_{0.3}O₉ ($0.1 \leq x \leq 0.5$) compounds were prepared by the sol-gel method using Lanthanum nitrate La(NO₃)₃·6H₂O, ammonium molybdate (NH₄)Mo₇O₂₄·4H₂O, dysprosium Nitrate Dy(NO₃)₃·6H₂O, and ammonium metatungstate (NH₄)₆H₂W₁₂O₄₀. All chemicals were procured from Sigma Aldrich USA with 99.9% purity and used without further purification. Lanthanum nitrate and ammonium molybdate were dissolved in double distilled water in a 1 : 1 molar ratio. Then, stoichiometric amounts of dysprosium nitrate and ammonium metatungstate were added under rigorous stirring. The stirring was continued till the formation of a uniform milky white color solution. Then the pH of solution was adjusted to 2 by the addition of 2.0 mol L⁻¹ solution

of nitric acid. The solution was kept in a water bath at 60 °C till gelation was completed. The entire process took around 40 to 48 hours. The white substance formed was crushed in a mortar and dried at 120 °C for 24 hours. The dried powder was annealed at 700 °C for 4 hours (optimized conditions). The same procedure was repeated to prepare the systems having different compositions of Dy by substituting La. The compositions developed in the study were nomenclatured as $\text{La}_2\text{Mo}_2\text{O}_9$ (LMX), $\text{La}_{1.9}\text{Dy}_{0.1}\text{Mo}_{1.7}\text{W}_{0.3}\text{O}_9$ (LMXD-1), $\text{La}_{1.8}\text{Dy}_{0.2}\text{Mo}_{1.7}\text{W}_{0.3}\text{O}_9$ (LMXD-2), $\text{La}_{1.7}\text{Dy}_{0.3}\text{Mo}_{1.7}\text{W}_{0.3}\text{O}_9$ (LMXD-3), $\text{La}_{1.6}\text{Dy}_{0.4}\text{Mo}_{1.7}\text{W}_{0.3}\text{O}_9$ (LMXD-4), and $\text{La}_{1.5}\text{Dy}_{0.5}\text{Mo}_{1.7}\text{W}_{0.3}\text{O}_9$ (LMXD-5).

The structure of the as-annealed sample was confirmed by the X-ray diffraction technique using a BRUKER D8 Advance diffractometer with a Cu $K\alpha$ source and 1-D position sensitive detector (LynsEye) based on the silicon drift detector technique. The XRD patterns were fit with Rietveld refinement techniques using Full Prof software and a 3D view of the crystal structure was generated by using VESTA program. For electrical characterization, the powder samples were pressed into a disc shaped pellet of 13 mm diameter. The pelletized samples were sintered in air by controlled microwave heating at 1000 °C for 30 minutes (optimized conditions). The sintering effect on the structure was revealed from the XRD of the sintered pellets of all co-doped LMX systems. The sintered pellets were silver painted on both sides for electrical characterization. An impedance spectrum was measured using Metrohm autolab model 204. The measurement conditions were as follows: (i) temperature range 300–700 °C and (ii) frequency range 1 Hz–1 MHz with an AC single of 20 mV in the air. Electric modulus data were extracted from impedance data. The dielectric measurements of the pure and co-doped LMX systems were done using Wyne-Ker made LCR meter model 4100. Raman spectroscopy was carried out with a Jobin

YVON Horiba LABRAM-HR-Visible system equipped with a He–Ne laser (633 nm) as the source and CCD detector with an overall spectral resolution of 1 cm^{-1} . The temperature was varied by keeping the sample in a LINKAM, UK made sample stage for a temperature range of 30–650 °C.

3. Results and discussion

3.1 X-ray diffraction

Fig. 1 shows the XRD patterns of all compositions of the co-doped LMX system. There are detectable changes in the XRD patterns of the LMX-pure and co-doped systems. It is observed that the XRD patterns of the LMX-pure and LMXD-1 systems exhibit a splitting of the reflections of characteristic peaks (211), (200), and (231) which are consistent with the monoclinic distortion in the α -phase. For more structural clarity, a magnified view of the XRD patterns near (211), (200) and (231) is presented in inset Fig. 1b–d. The splitting of the diffraction peaks (211), (200) and (231) at around $2\theta = 30\text{--}32^\circ$, $41\text{--}43^\circ$ and $47\text{--}51^\circ$ can be clearly observed for pure-LMX and LMXD-1 systems. However, no peak splitting is detected for the LMXD-2, LMXD-3, LMXD-4 and LMXD-5 samples. The splitting of peaks indicates a low symmetry phase of LMX and LMXD-1 and can be related to the monoclinic α -phase,^{40–43} while a cubic β -phase is indicated for the co-doped LMX system (except LMXD-1). LMXD systems having a Dy content $x = 0.4$ and 0.5 show the existence of impurity phases ($\text{La}_2\text{Mo}_3\text{O}_9$). The variation of the lattice parameters as a function of Dy content is displayed in Fig. 1(e). There are systematic reductions in the lattice parameter with Dy content. These reductions can be attributed to the incorporation of the smaller Dy^{3+} ion ($r = 0.912 \text{ \AA}$ at CN = 6) into a larger La^{3+} ($r = 1.032 \text{ \AA}$ at CN = 6) lattice site in $\text{La}_2\text{Mo}_2\text{O}_9$.

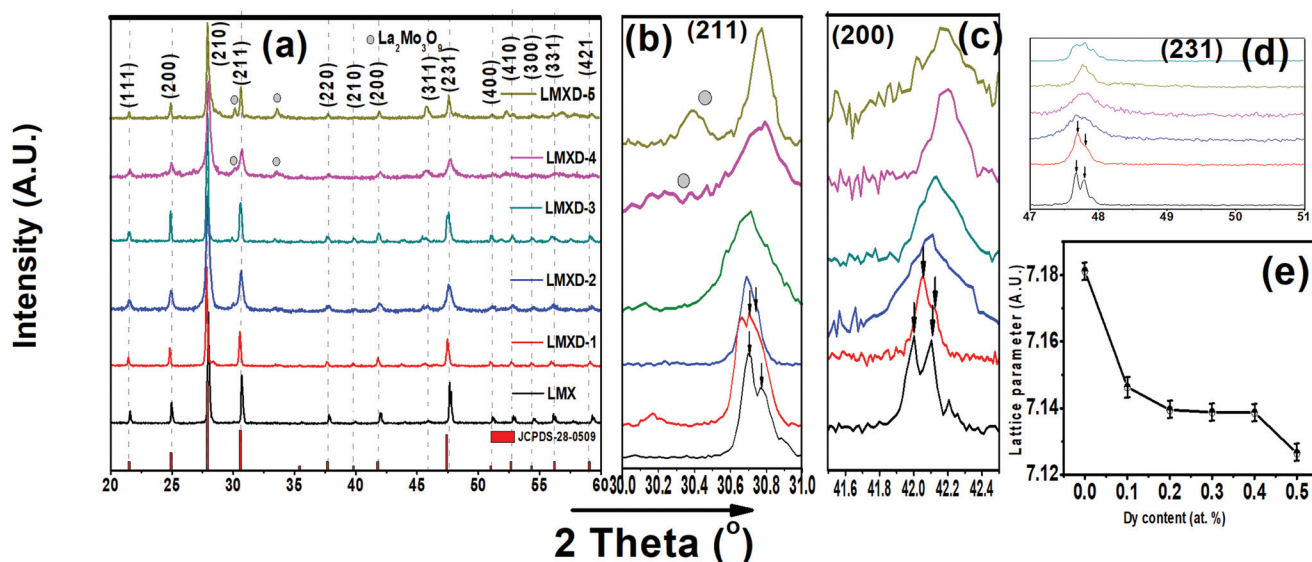


Fig. 1 (a) XRD patterns of all co-doped compositions of LMX, (b) a magnified view of the (211) peak, (c) magnified view of the (200) peak (d) magnified view of the (231) peak, and (e) lattice parameters as a function of Dy content.

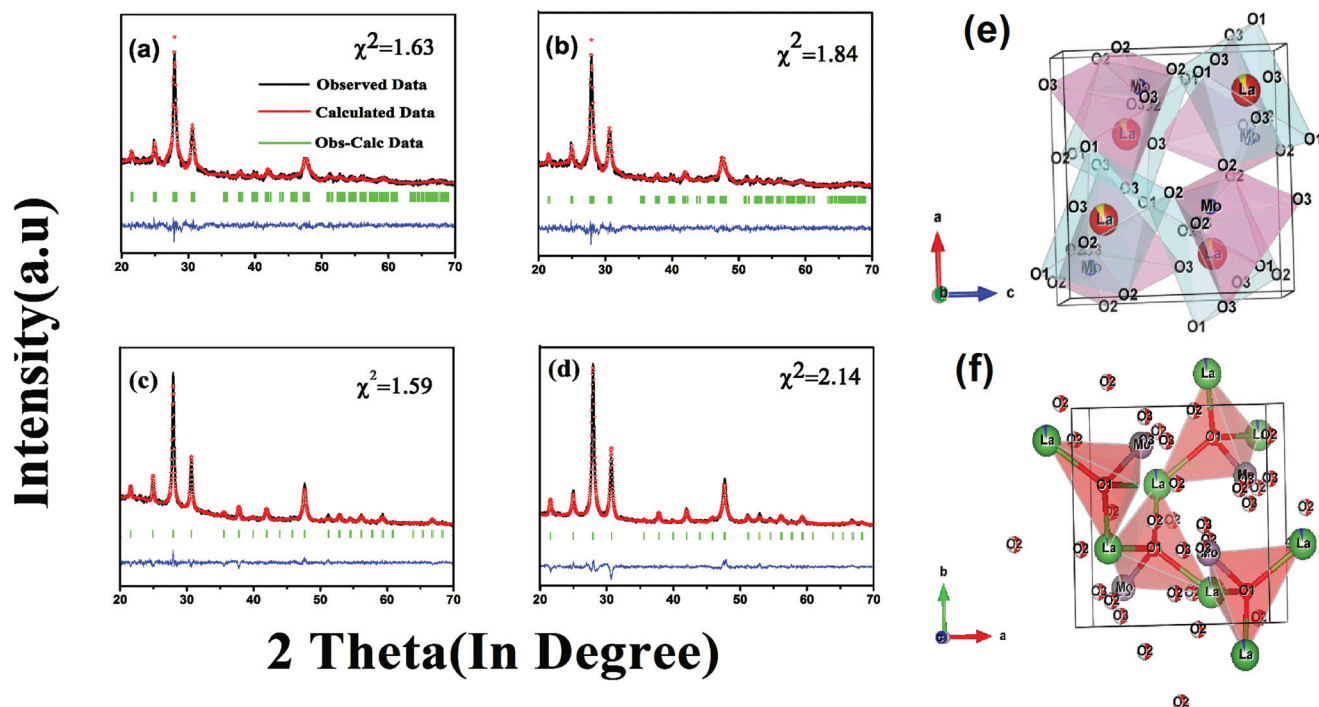


Fig. 2 Rietveld refined file (a) LMX, (b) LMxD-1, (c) LMxD-2, and (d) LMxD-3, (e) and (f) 3D view of LMxD-3.

The diffraction patterns of a few compositions are derived from Rietveld refinement and displayed in Fig. 2. The reflections of the pure-LMX and LMxD-1 systems are indexed using monoclinic symmetry with the space group $P2_1$, while all other co-doped samples are indexed by the $P_{2,3}$ space groups of the cubic β -LMX phase. The geometric view of the LMX unit cell designed by using VESTA program from the extracted data of Rietveld refinement is displayed in Fig. 2(e and f).

Fig. 3 shows the SEM micrographs of LMxD-3 (a representative system) displaying a highly compacted structure with well-defined grain boundaries. The relative densities of all microwave sintered samples are around 92–95%. The statistical analysis of particle size made on these micrographs indicates an average particle size of about 1 to 2 μm . The same trends of microstructure are observed for almost all co-doped LMX compositions, as all are compacted under the same conditions.

3.2 Raman spectroscopy

Raman spectroscopy is a powerful tool to probe local ordering-disordering of crystalline lattice or defects. In the LMX system, α to β -phase transition is accompanied by a transition from a static to a dynamic distribution of oxygen defects.⁴⁰ So, Raman spectroscopy is used to closely monitor the distribution of the oxygen defect, role of co-dopant in the re-distribution of oxygen defects and accompanied phase transition, and oxy-ion diffusion dynamics. The Raman spectra of four representative co-doped LMX systems (LMX, LMxD-1, LMxD-2, LMxD-3) are shown in Fig. 4. For the interpretation of Raman spectroscopic data, previous studies on Raman spectra for both the monoclinic and the cubic phases are used.^{44–49}

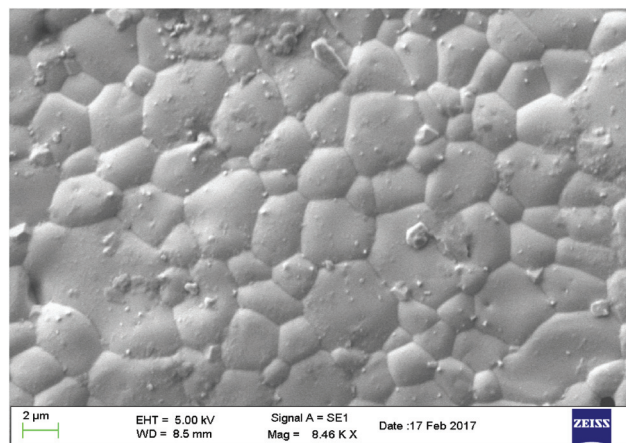


Fig. 3 Micrograph image of a compacted pellet of LMxD-3.

Vibration mode representations for the monoclinic and cubic phases at the center of the Brillouin zone are as follows:

Monoclinic

$$\Gamma_{\text{vibra}} = 25A_g + 25A_u + 26B_g + 26B_u$$

Acoustic and optic modes are

$$\Gamma_{\text{Acoustic}} = A_u + 2B_u$$

$$\Gamma_{\text{vibra}} = 25A_g + 24A_u + 26B_g + 24B_u$$

Infrared and Raman active modes are

$$\Gamma_{\text{Raman}} = 25A_g + 26B_g$$

$$\Gamma_{\text{infrared}} = 25A_u + 26B_u$$

Cubic

$$\Gamma_{\text{optic}} = 10A + 20E_{1,2} + 29T$$

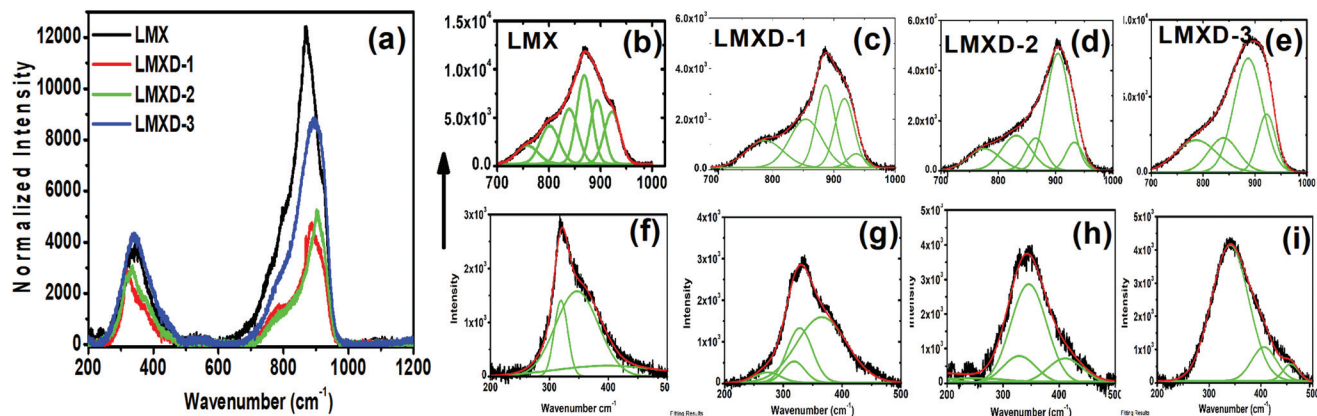


Fig. 4 (a) Comparative room temperature Raman spectra of LMX, LMXD-1, LMXD-2, and LMXD-3, (b–i) deconvoluted spectra at low and high wavenumber range of respective system.

However, the total numbers of experimentally observed peaks are significantly lower than that of predicted symmetry 59 for cubic and 51 for monoclinic which is common for polycrystalline samples with a large number of atoms in a unit cell.^{50,51} The Raman spectra of all systems can be divided into two parts with a wide empty gap in the range of 500–700 cm^{-1} , which are commonly observed in molybdates with MoO_4 tetrahedra. In the range of the stretching vibration of MoO_n polyhedra (720–920 cm^{-1}), many lines were observed because of the presence of several independent and distorted MoO_4 tetrahedra. Noticeable changes are detectable in the Raman modes of the co-doped LMX counter-part to parent system (see Fig. 4) *viz* (i) drop in peak height, (ii) peak splitting and (iii) shift in peak position. The disappearance of a few peaks can be associated with either suppression or merger of the corresponding bond vibration. The peak height of the Raman mode can be used to estimate the strength of the lattice ordering and the peak shift is directly related to crystal symmetry. The extracted data of peak height and peak shift of the Raman mode can be used to evaluate lattice ordering–disordering and crystal symmetry, respectively. To interpret the Raman spectra more precisely, we have deconvoluted all spectra.^{52–55} The deconvolution method was performed using Origin-Pro 8.5 software. The Raman spectrum was deconvoluted using the Gaussian fitting function. The details of the deconvolution procedure are provided in the ESI.† The semi-quantitative information of Raman modes *i.e.* the peak position, peak height, and peak width, are extracted-out from the deconvoluted Raman spectra. We had performed the deconvolution very carefully by keeping the percentage error of fitting less than 1%. The deconvoluted spectra in high wavenumber range (700 to 1000 cm^{-1}) and low wavenumber range (200–400 cm^{-1}) are separately analyzed: (see panel Fig. 4b–i)

3.2.1 Room temperature Raman spectra. (i) In pure LMX, several modes are observed in a high wavenumber range (700 to 1000 cm^{-1}); amongst these prominent modes are at around 758 cm^{-1} , 808 cm^{-1} , 870 cm^{-1} and 922 cm^{-1} , respectively. The Raman vibration mode detected near 870 cm^{-1} and 922 cm^{-1}

can be assigned to the $\text{Mo}_1\text{–O}_1$ and $\text{Mo}_1\text{–O}_2$ symmetric stretching (ν_1) vibration, respectively.⁵⁶ The modes near 758 cm^{-1} and 808 cm^{-1} are assigned to the $\text{Mo}_1\text{–O}_1$ and $\text{Mo}_1\text{–O}_2$ asymmetric stretching (ν_3) vibration.

(ii) In the co-doped LMXD-1 system, four prominent deconvoluted modes having comparable intensity are detected at 775, 855, 886 and 903 cm^{-1} . The Raman modes of LMXD-1 are found to be shifted in the high wavenumber side with a 50% drop in peak height as compared to the pure LMX system.

(iii) In the case of the LMXD-2 system, deconvoluted modes are observed near 775, 831, 865, 903 cm^{-1} , while the intensity of the modes is suppressed as compared to 903 cm^{-1} . The peak height of the mode drops by almost 70% as compared to pure LMX.

(iv) For the LMXD-3 system, a single dominant peak near 903 cm^{-1} is related to the symmetric stretching (ν_1) vibration; however the intensity of the peak drops more than in the LMX system.

(v) Lower wavenumber side Raman spectra reveal two noticeable modes for LMX (at around 335 and 440 cm^{-1}) and LMXD-1 (318 and 369 cm^{-1}), while a single prominent peak is detected for LMXD-2 (333 cm^{-1}) and LMXD-3 (339 cm^{-1}). The band near 335 cm^{-1} in LMX can be assigned to the symmetric bending (ν_2) vibration mode and the band located near 440 cm^{-1} can be associated with the asymmetric bending (ν_4) vibration of Mo–O in the MoO_4 tetrahedral unit.

The few prominent changes observed in the Raman spectra due to co-dopants in the LMX systems are: a decrease in peak height and the disappearance of a few modes. The suppression in peak height indicates a weakening of the Raman mode related to Mo–O vibrations caused by the delocalization of the lattice oxygen ion or the formation of disordered oxygen vacancies defects, while the disappearance of a few Raman modes is due to deformation in the MoO_4 tetrahedral unit. The structural changes and accompanied oxygen ion re-distribution as observed by XRD and Raman spectroscopy, respectively, in the co-doped LMX systems confirm that the $\alpha \rightarrow \beta$

structural transition precedes the re-distribution of oxygen ions or vacancies.

3.2.2 High temperature Raman spectra. High temperature Raman spectra of LMXD are monitored at various temperatures between 27 and 600 °C (more specifically, 27, 100, 200, 300, 350, 400, 450, 500, 550, 580, 600 °C) to reveal modifications in local structural changes and their influence on the oxy-ion diffusion mechanism; Fig. 5(a–d) shows normalized high temperature Raman spectra of LMX, LMXD-1, LMXD-2, LMXD-3 systems, respectively. Detectable changes in peak intensity and peak shape as a function of temperature can be visualized in the inset view of the spectra, (except LMXD-3); however peak shift is almost negligible.

To reveal the phase transition influence on the Raman spectra, the deconvoluted Raman modes of the LMX and LMXD-1 systems are closely monitored near the transition temperature (550–600 °C, see ESI Fig. S-1†). A few lines of the Raman modes start disappearing near the phase transition temperature *i.e.* above 550 °C. The disappeared lines are related to the Mo–O bond stretching and bending vibrations, indicating dislocation of oxygen ions from the Mo nearest position upon changing its coordination number.

To extract temperature induced relative changes in the Raman spectra, peak height data are collected from deconvoluted spectra and plotted as a function of temperature; a few prominently varying modes are displayed in Fig. 6; *i.e.* four modes of LMX and LMXD-1 systems and two modes of LMXD-2 and LMXD-3. As the Raman modes are associated with the lattice vibration of oxygen (O) with respect to Mo, the peak height measures the strength of the lattice ordering. The peak height is found to vary irregularly with the temperature correlating to the disordering of oxygen ion or oxygen vacancies and can be associated with dynamical disordering in the LMXD lattice.

3.3 Dielectric analysis

Dielectric relaxation phenomenon as a function of temperature is systematically studied and displayed in Fig. 7(a–g). The dielectric relaxation or tangent of the loss angle ($\tan \delta$) is

mainly measured by the electrical energy dissipated during a reorientation of dipoles due to the electric field. The theory of point defect relaxation predicts that the square of the dipole shape factor is based on the concept that each point defect, *e.g.*, vacancy, creates an elastic or electric dipole and the relaxation strength has a linear dependence on the defect concentration.⁵⁷ In the LMX system, point defects are mainly oxygen vacancies that are evolved in the dielectric phenomenon.

The results of dielectric relaxation were obtained at a heating rate of 3 °C min⁻¹ and the system was stabilized at a particular temperature for 30 min before the reading was taken. The study was repeated at various frequencies between 1 and 50 kHz. Fig. 7a shows the comparative dielectric relaxation curve as a function of the temperature of all six LMX co-doped systems at 2 kHz. The co-dopant effect on the dielectric loss and relaxation mechanism can be clearly visualized: (i) The peak height (strength) of the dielectric relaxation curve is more in LMXD than in LMX, (ii) There are two dielectric relaxation mechanisms for LMXD, while there is a single relaxation curve for pure-LMX. As the dielectric relaxation strength is linearly dependent on the defect concentration,⁵⁷ there is an indication that defect (oxygen vacancies) concentration is manipulated by Dy content in the LMX system. The role of Dy in enhancing the oxygen vacancy concentration is understood as Dy, W induced $\alpha \rightarrow \beta$ phase transition and an accompanied re-distribution of oxygen ion/vacancies in LMX (as evidenced from XRD, Raman spectroscopy) modifying the defect concentration.⁵⁸

The dielectric relaxation mechanism of the LMX-pure system at different frequencies 1, 2, 5, 10, 20 and 50 kHz, respectively is displayed in Fig. 7b. In all spectra, a prominent single relaxation peak is observed in a temperature of around 400 °C, which is found to be systematically suppressed with increasing frequency. This is the common dielectric feature of the LMX-pure system.⁵⁸ The existence of a single dielectric relaxation peak indicates a single relaxation frequency (/time) associated with the reorientation of oxygen vacancies in the system. In solid electrolytes, the oxygen vacancy defect reorientation leads to oxy-ion hopping *via* vacancies and thus ionic

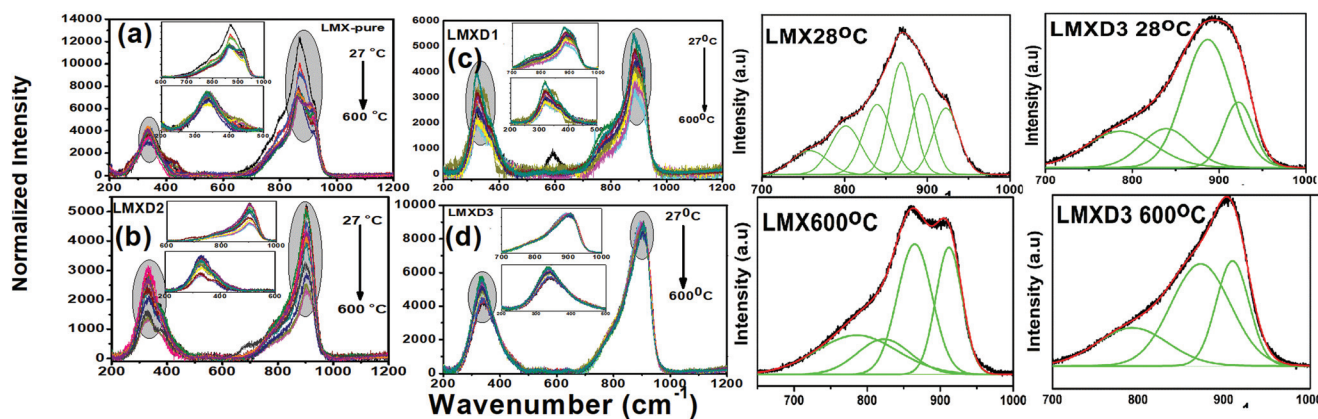


Fig. 5 High temperature Raman spectra (27–600 °C) of (a) LMX, (b) LMXD-1, (c) LMXD-2 and (d) LMXD-3 with deconvoluted spectra at 27 °C and 600 °C of the represented spectra system LMX and LMXD-3.

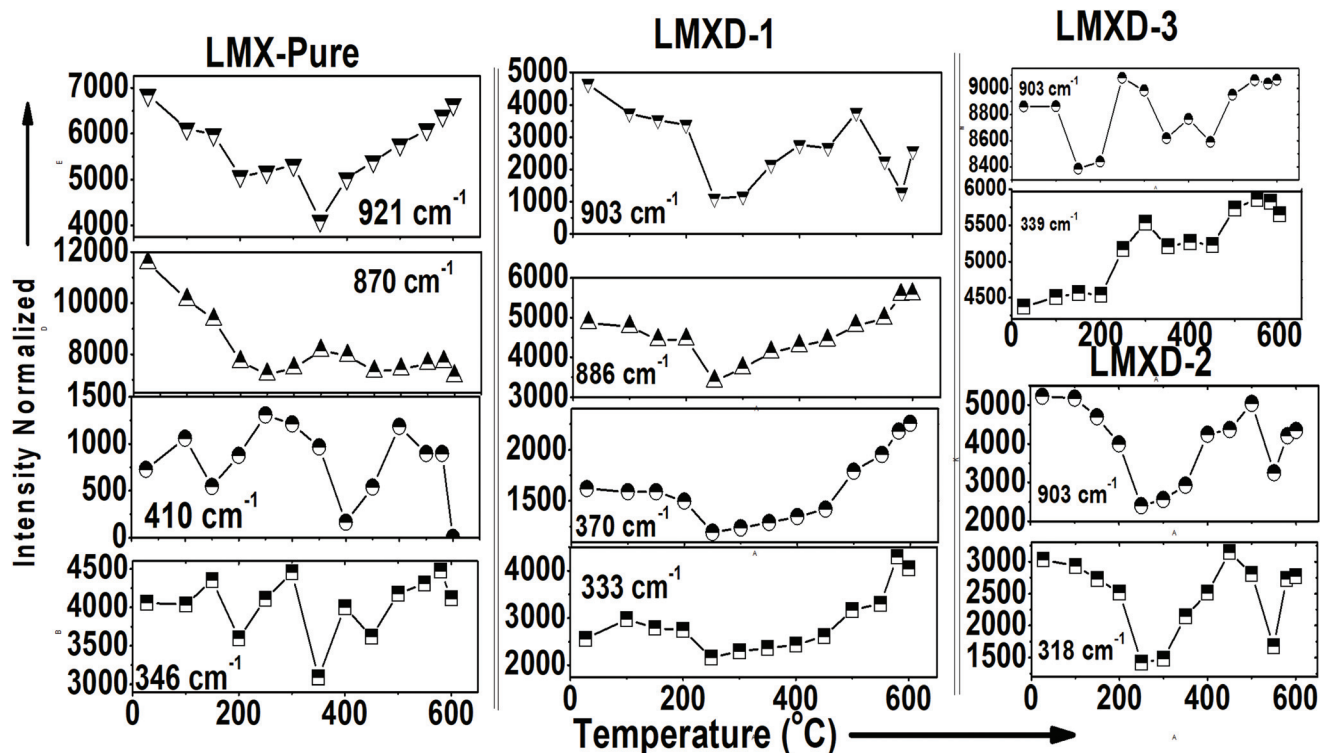


Fig. 6 A comparative intensity plot of a few prominent Raman modes of the LMXD system as a function of temperature.

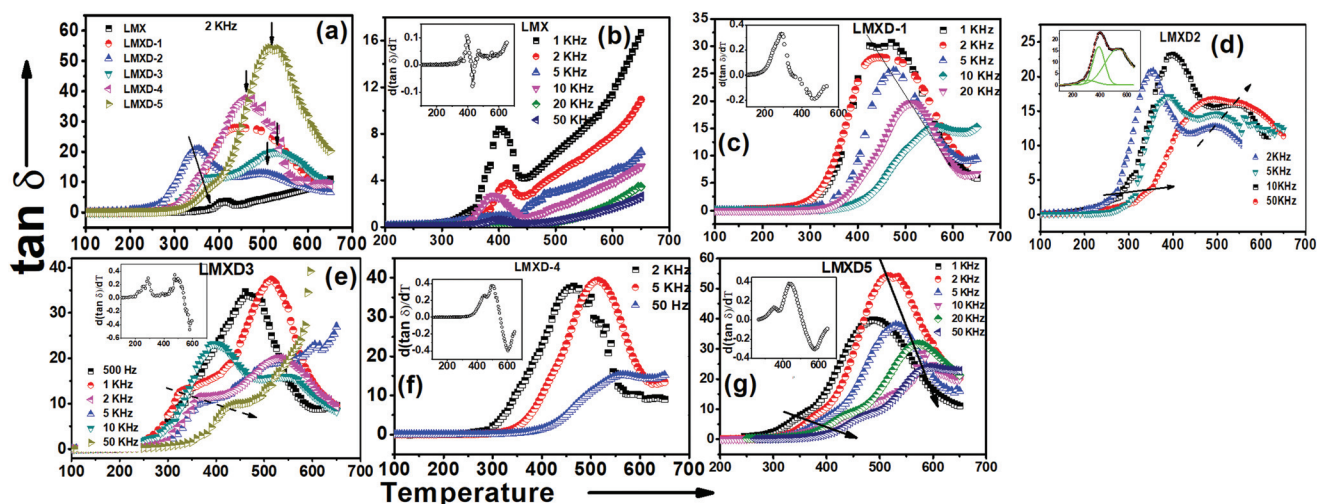


Fig. 7 Dielectric relaxation phenomenon as a function of temperature of (a) a comparison of dielectric loss spectra of co-doped LMX, (b) LMX (c) LMXD-1, (d) LMXD-2, (e) LMXD-3, (f) LMXD-4, and (g) LMXD-5.

conductivity.⁵⁹ The long range ordering of oxygen vacancies in α -LMX leads to a single relaxation frequency of oxygen ion hopping.

Dielectric relaxation curves of the LMXD-1, LMXD-2, LMXD-3, LMXD-4 and LMXD-5 systems (see Fig. 7c–g, respectively) exhibit two relaxation peaks in the temperature interval 350–550 °C. The relaxation peaks are shifted towards a high temperature side with increasing frequency, and this dielectric

relaxation phenomenon can be ascribed to a thermally activated process. The existence of more than one dielectric relaxation peak indicates multiple relaxation phenomena due to randomly distributed oxygen vacancies. In the β -LMX phase, La and Mo cations are located at 4a positions, alternating to form a lattice of slightly distorted parallelepipeds. Oxygen O₁ positions (4a sites) are fully occupied, and the oxygen O₂ positions and O₃ positions (12b) are partially occupied.⁴⁰

Therefore, oxygen vacancy defects are formed at the O₂ and O₃ sites. Thus, two dielectric relaxation peaks can be associated with the dielectric relaxation of oxygen vacancies from the O₂ and O₃ sites. Due to the high oxygen vacancy concentration in the sites of O₂ and O₃, the possibility of migration of oxygen ions from O₁ to O₂ and O₃ is large enough to produce a relaxation peak. Therefore, the migration processes of oxygen ions would give rise to two dielectric relaxation peaks when an oscillating electric field is applied.

3.4 Correlation of dielectric relaxation, dynamic ordering and Raman vibration mode anomalies

To demonstrate the dynamics of the disordering of oxygen vacancies and their correlation to the oxygen ion hopping mechanism, the derivative plot of the peak height of a few Raman modes of the Mo–O bond vibration (dI/dT) and dielectric relaxation ($d(\tan\delta)/dT$) as a function of temperature is studied (see Fig. 8a–d). dI/dT measures the rate of change of the ordering strength of oxygen ions with Mo, which is associated with the formation of oxygen vacancies. The non-uniform variations of dI/dT indicate a dynamic disordering of oxygen vacancies and the observed sharp anomaly in dI/dT can be related to a dynamically disordered state.

For pure-LMX, the derivative plot dI/dT vs. T of symmetric stretching (near 870 cm⁻¹) and the bending Raman mode (near 346 cm⁻¹) of Mo–O vibration are shown (see Fig. 8a). Both the modes exhibit a non-uniform variation of dI/dT as a

function of temperature (100–600 °C); while the $d(\tan\delta)/dT$ curve shows an anomaly around 400 °C; the temperature range of dielectric relaxation is the same as that for oxygen ion diffusion in oxide ceramics.^{60,61} The mechanism of diffusion of oxygen ions *via* vacancies is confirmed and associated with the diffusion process between O(1), O(2) and O(3) orderly arranged vacancies sites.⁶² Moreover, dielectric relaxation is not accompanied by a dynamically disordered state in pure-LMX.

For the co-doped system, derivative plots, *i.e.*, dI/dT and $d(\tan\delta)/dT$, display two sharp anomalies at around the same temperature, signifying that dynamically disordered states are correlated to oxygen vacancy relaxation dynamics. According to the thermodynamic selection rule for point defect relaxation, oxygen ion-vacancy exchange diffusion processes occur due to those point defects whose symmetry is lower than that of the crystal. In the cubic LMX crystal, all of the oxygen sites have lower symmetry. Therefore, a dielectric loss peak results from an oxygen ion-vacancy exchange diffusion process between randomly distributed oxygen vacancies mainly attribute to the jumps between the nearest neighbor O(1) → O(2) and O(1) → O(3) sites.

3.5 Electrical properties

To ascertain the bulk relaxation response of moderately conducting materials, complex electric modulus formalism is an important tool. Relaxation dynamics and activation energy for

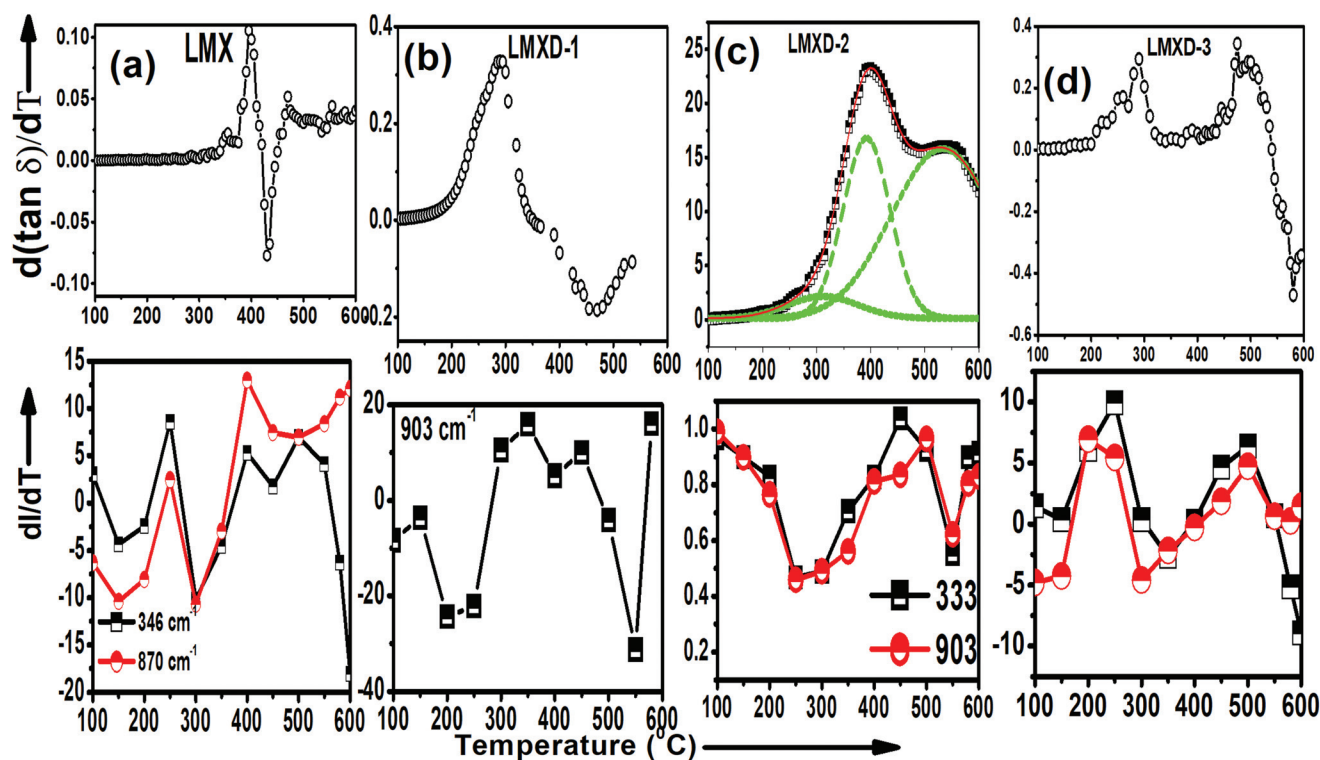


Fig. 8 Derivative plot of dissipation factor and intensity of the Raman mode with respect to temperature (a) LMX, (b) LMxD-1, (c) LMxD-2, (d) LMxD-3.

oxy-ion transport *via* oxygen vacancies in the matrix of the co-doped LMX can be calculated from the modulus plot. At lower frequencies, there is an exponential increase in the dielectric constant and loss; also, there is difficulty in distinguishing the interfacial polarization and conductivity contribution from intrinsic dipolar relaxation. Such a difficulty is overcome by representing the data in electric modulus formalism.

The imaginary part of the electric modulus M'' , which is indicative of the energy loss under the electric field, is highly sensitive to understanding a temperature induced bulk relaxation response. The normalized modulus spectra (M''/M''_{\max}) for $x = 0-0.5$ at intermediate temperatures (400 °C–700 °C) are studied (Fig. 9a–f). The normalized spectra of the imaginary modulus are fit with the Bergman function represented by

$$M'' = \frac{M''_{\max}}{1 - \beta + \left(\frac{\beta}{1 + \beta}\right) \left[\beta \left(\frac{\omega_{\max}}{\omega}\right) + \left(\frac{\omega}{\omega_{\max}}\right)^{\beta}\right]}$$

where M''_{\max} represents the broadness of the spectra. For all samples, β -values that are found to be less than 1 indicate deviation from the Debye-type relaxation. From Fig. 9a, it is observed that the relaxation peak is found to shift towards the high-frequency side with the rise in temperature which confirms that the relaxation dynamics are thermally activated. This temperature dependent behavior of M'' can be elaborated as the charge carrier gets thermally activated with an increase in the temperature and they acquire rapid movement. This leads to a decrease in the relaxation time and hence increases in relaxation frequency. It can be noted that the separation between

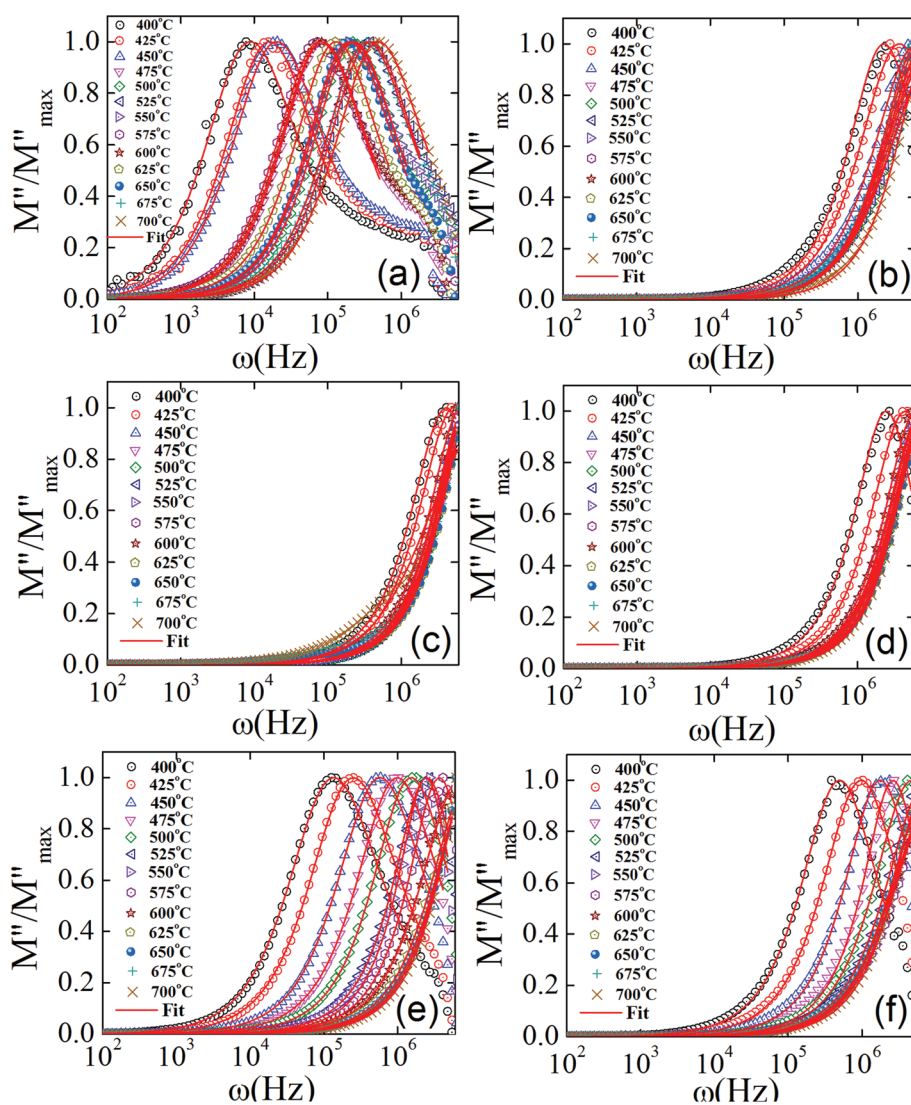


Fig. 9 Normalized modulus spectra (M''/M''_{\max}) for $x = 0-0.5$ at intermediate temperatures (400 °C–700 °C) of (a) LMX, (b) LMXD-1, (c) LMXD-2, (d) LMXD-3, (e) LMXD-4, (f) LMXD-5.

relaxation peaks with the elevation of temperature for the samples with the composition $x = 0$, $x = 0.4$ and $x = 0.5$ is large, whereas less separation and relaxation peaks are found from the window of measuring frequency for the $x = 0.1$, $x = 0.2$ and $x = 0.3$ samples. The large separation between the relaxation peaks is influenced by a short-range motion of charge carriers (within grains). The f_{\max} value is calculated from the relation $\omega_{\max} = 2\pi f_{\max}$. The f_{\max} value is temperature-dependent and follows the Arrhenius equation; $f_{\max} = f_0 e^{-\frac{E_a}{kT}}$ whereas f_0 is the pre-exponential factor, E_a is the activation energy, and k is the Boltzmann constant. Fig. 10(a–f) shows the Arrhenius plots for all samples. A discontinued jump in $\ln(f_{\max})$ for the parent compound is observed around the α - β transition temperature (~ 560 °C). The activation energy, E_a below the transition temperature (< 560 °C) is found to be 1.49 eV, whereas above 560 °C, the E_a reduce to 1.32 eV. These activation energies can be correlated to the migration of oxygen vacancies. Thus, the movements of oxygen vacancies in the high-temperature β phase experience less hindrance than in the α phase.⁶⁶ The activation energy (E_{a2}) corresponding to the temperature < 560 °C exhibits a detectable decrease in the low

doping level of Dy ($x = 0.1$ – 0.3) while it enhances upon further substitution ($x = 0.4$ – 0.5).

The ionic conductivity data are extracted from complex impedance spectra (Z'' vs. Z'). We collect the impedance spectra of the co-doped LMX system at various temperatures under air atmosphere. It is the most suitable technique to distinguish the grain, grain boundary, and the electrode effect Fig. 11 depicts the impedance spectra of various compositions at 400 °C with the fit equivalent ckt at the inset of each spectrum. The equivalent circuit exhibits three semicircles fit in high, intermediate and low frequency ranges. The circuit consists of Resistance R and pseudo-capacitance CPE. The total circuit can thus be expressed as (R_g, CPE_g) , (R_{gb}, CPE_{gb}) and (R_e, CPE_e) , where g , gb and e stand for grain/bulk, grain boundary and material/electrode interface, respectively. These contributions are confirmed from the capacitance values that are of pF range in the grain/bulk region, nF range grain boundary region and μ F range in the electrode region. However, the equivalent circuits of almost all specimens of LMX except that of LMXD-3 exhibit an inductive reactance at the high frequency side. This can be attributed to the electronic conductivity

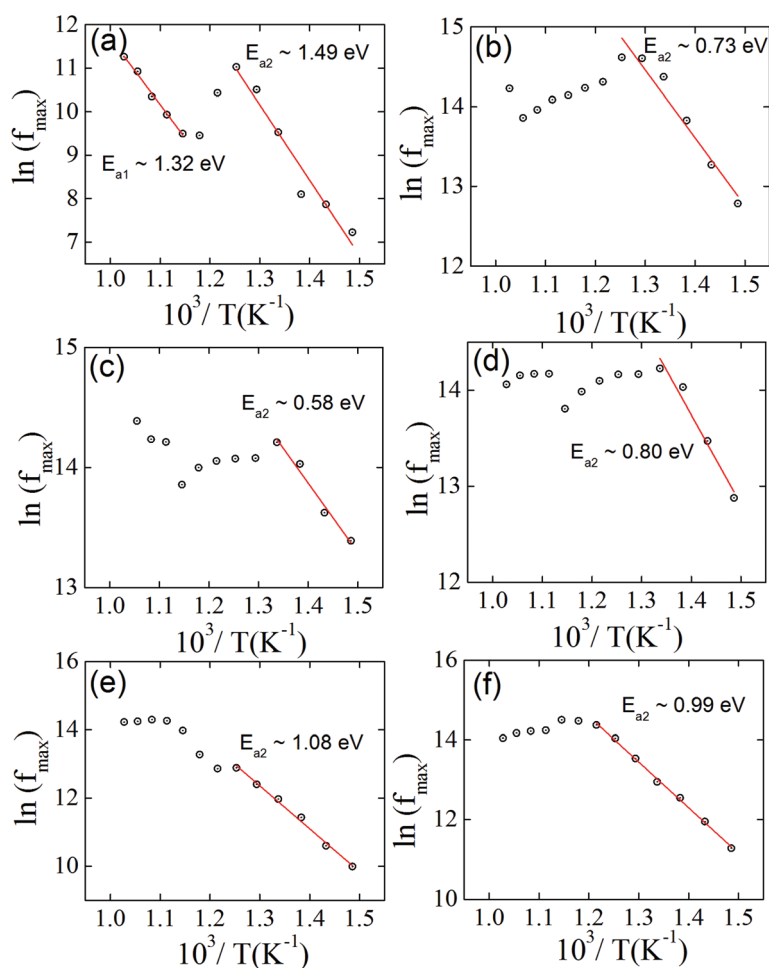


Fig. 10 Arrhenius plot ($\ln(f_{\max})$ versus temperature) of the co-doped LMX samples (a) LMX-pure, (b) LMXD-1, (c) LMXD-2, (d) LMXD-3, (e) LMXD-4 and (f) LMXD-5.

across the grain/bulk region because the ion conductivity of the LMX compound at 400–700 °C is of main interest for IT-SOFC electrolyte applications. The experimental conductivity σ of the ceramic specimens was calculated from the interceptions of the observed semicircle on the real axis Z' of the impedance plot. The impedance spectra above 600 °C do not show a high frequency arc (>1 MHz). The extrapolated results of grain contribution are used to determine grain resistance.

Fig. 11(f) shows the Arrhenius plot of $\log \sigma$ as a function of $1000/T$ for the specimens. The fit line reveals that the conductivity data obey the Arrhenius law well in the measured temperature range for all Dy and W co-doped LMX specimens. However for LMX, a jump of conductivity around 575 °C is observed due to a structural $\alpha \rightarrow \beta$ phase transition. This indicates that substituting Dy^{3+} for La^{3+} and W^{6+} for Mo^{6+} could suppress the first order phase transition of LMX and stabilize the cubic structure at room temperature.

In an earlier study, Tsu-Yung Jin *et al.*⁶⁷ and S. Georges *et al.*³⁸ have reported a switching of Arrhenius to Vogel–Tamman–Fulcher (VTF) behavior in temperature dependence ionic conductivity, especially in the high temperature range in Dy, W co-doped LMX and W-doped LMX systems. The high temperature non-Arrhenius behavior has been understood as ion diffusion by thermally assisted lattice motion. However, we obtain Arrhenius behavior for a temperature range of 400–700 °C, which is the operating temperature range of IT-SOFCs. The conductivity of the LMXD-2 and LMXD-3 systems exceeds that of pure LMX (see inset Fig. 11(f)). In general, the conductivity values of the LMX samples obtained in this work (7.2×10^{-3} @700 °C to 3.4×10^{-3} S cm^{-1} @500 °C

of LMX) are close to those reported earlier in the literature;^{68,69} while the conductivity of LMXD-3 (1.03×10^{-2} @700 °C and 6.32×10^{-3} @500 °C) is more than the value reported for a similar system.^{66,67,70} The activation energy (E_a) of the total conductivity varies as 0.98 eV for LMXD-3 to 1.20 eV for the LMXD-5 system showing good consistency with the nature of oxy-ion conductivity. Therefore, the Dy and W substituted LAMOX have the merit of high ion conductivity. The E_a values for the Dy-doped samples are relatively lower than those of the parent sample, except LMXD-5.

In summary, the Dy, W co-dopant effects on the suppression of the $\alpha \rightarrow \beta$ phase transition of the LMX system are confirmed by the disappearance of the splitting of peaks (211), (200) and (231), which are clearly observed for LMX-pure at around $2\theta = 30\text{--}32^\circ$, $40\text{--}42^\circ$ and $47\text{--}48^\circ$, respectively. Raman spectroscopic data support the suppression of the monoclinic-to-cubic phase of the co-doped-LMX by the disappearance of a few Raman vibration modes related to MoO_4 tetrahedral distortion with asymmetric stretching and bending vibration, which are obtained in the parent system. High temperature Raman spectra demonstrate the existence of a dynamical disorder in the co-doped LMX system by a non-uniform variation of dI/dT as a function of temperature. The dynamically disordered states are found closely associated with dielectric relaxation. The single dielectric relaxation phenomenon is observed in the pure LMX system, while two dielectric relaxations are detected for co-doped LMX. The dynamics of oxygen ion diffusion is understood from dielectric relaxation. In the Dy–W co-doped system, two dielectric relaxation peaks are observed to be associated with two dynamically disordered states and originate from a diffusion process between O(1)–O(2) and

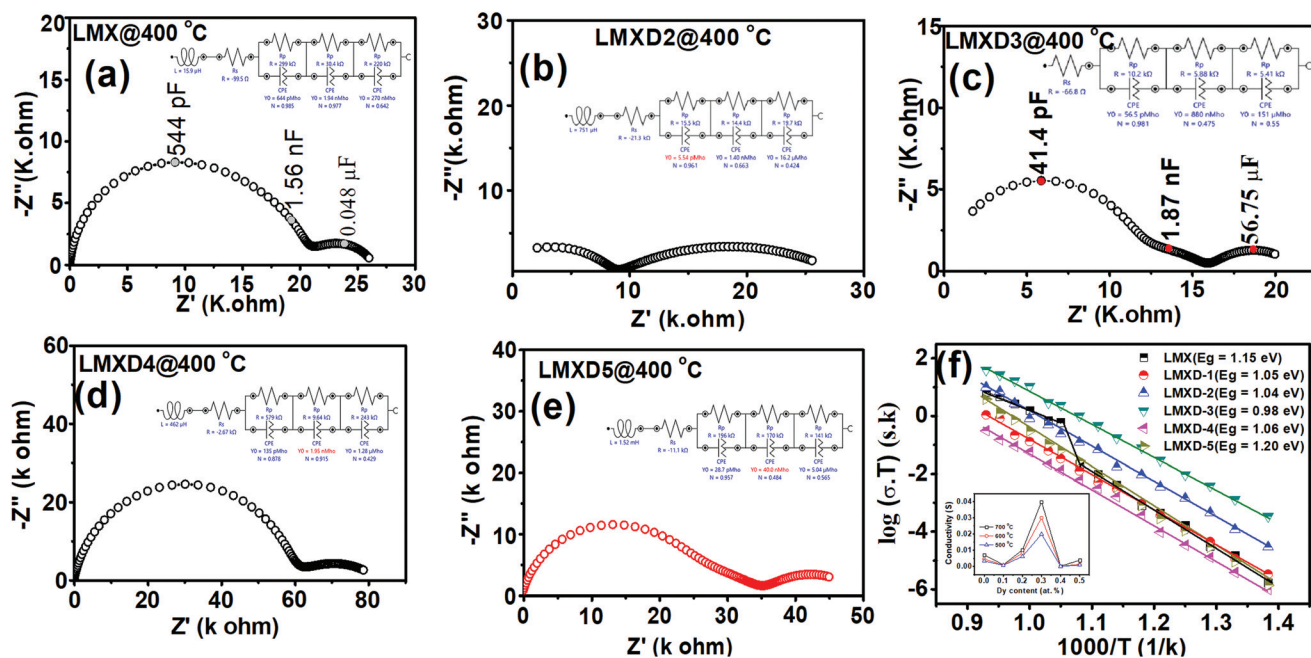


Fig. 11 Impedance spectra@400 °C of the Dy, W co-doped LMX system (a) LMX-pure, (b) LMXD-2, (c) LMXD-3, (d) LMXD-4, (e) LMXD-5 and (f) Arrhenius plot.

O(1)–O(3) oxygen ion-vacancies sites. Electric modulus spectra ascertained from the non-Debye type relaxation dynamics and activation energy of ion migration in co-doped LMX are lower than that of the parent system. Ionic conductivity data extracted from the complex impedance plot exhibit a single slope Arrhenius behavior of Dy and W co-doping in LMX samples for the 400–700 °C temperature regime, while there is a jump in plot around 575 °C in pure LMX. There are reasonable increases in conductivity with a decrease in activation energy by the co-doping effect in the LMX samples. This study demonstrates the Dy, W co-dopant effect on the suppression of phase transition temperature and dynamical disordering of oxygen vacancies. It modifies the dielectric relaxation phenomenon and thus oxygen vacancy reorientation kinetics. It reduces the active energy for the migration of oxygen ions by improving conductivity; it proves the suitability of the co-doped LMX system to be used as electrolytes for intermediate temperature solid oxide fuel cells (400–700 °C).

Conflicts of interest

There are no conflicts to declare.

Acknowledgements

SAA acknowledges DST-SERB for funding through the Research project of file No. CRG/2018/002490.

References

- J. P. Fournier, J. Fournier and R. Kohlmueller, *Bull. Soc. Chim. Fr.*, 1970, **12**, 4277–4283.
- P. Lacorre, F. Goutenoire, O. Bohnke, R. Retoux and Y. Lalignant, Designing fast oxide-ion conductors based on $\text{La}_2\text{Mo}_2\text{O}_9$, *Nature*, 2000, **404**, 856–858.
- F. Goutenoire, O. Isnard, R. Retoux and P. Lacorre, Crystal structure of $\text{La}_2\text{Mo}_2\text{O}_9$ (LAMO), a new fast oxide-ion conductor, *Chem. Mater.*, 2000, **12**, 2575–2580.
- K. Huang, R. S. Tichy and J. B. Goodenough, Superior perovskite oxide-ion conductors; strontium and magnesium-doped LaGaO_3 :I, phase relationship and electrical properties, *J. Am. Ceram. Soc.*, 1998, **81**, 2565–2575.
- F. Yang, H. Zhang, L. Li, I. M. Reaney and D. C. Sinclair, High Ionic conductivity with Low degradation in A-site Strontium-doped Nonstoichiometric Sodium Bismuth Titanate Perovskite, *Chem. Mater.*, 2016, **28**, 5269–5273.
- N. Q. Minh, Ceramic fuel cells, *J. Am. Ceram. Soc.*, 1993, **76**, 563–588.
- T. H. Etsell and S. N. Fllengas, Electrical properties of solid oxide electrolytes, *Chem. Rev.*, 1970, **70**, 339–376.
- C. Ahamer, A. K. Opitz, G. Rup and J. Fleig, Revisiting the Temperature Dependent Ionic Conductivity of Yttria stabilized Zirconia (YSZ), *J. Electrochem. Soc.*, 2017, **164**(7), F790–F803.
- A. V. Shlyakhtina and L. G. Shcherbakova, New Solid Electrolytes of the Pyrochlore Family, *Russ. J. Electrochem.*, 2012, **48**, 3–30.
- K. J. Moreno, A. F. Fuentes, M. Maczka, J. Hanuza, U. Amador, J. Santamaria and C. Leon, Influence of thermally induced oxygen order on mobile ion dynamics in $\text{Gd}_2(\text{Ti}_{0.65}\text{Zr}_{0.35})_2\text{O}_7$, *Phys. Rev. B: Condens. Matter Mater. Phys.*, 2007, **75**, 184303–8.
- F. Abraham, J. C. Boivin and G. Mairesse, The BIMEVOX series: a new family of high performance oxide ion conductors, *Solid State Ionics*, 1990, **40/41**, 934–937.
- F. Abraham, M. F. Debreulle-Gresse, G. Mairesse and G. Nowogrocki, Phase transitions and ionic conductivity in $\text{Bi}_4\text{V}_2\text{O}_{11}$, an oxide with a layered structure, *Solid State Ionics*, 1998, **28–30**, 529–532.
- L. T. Sim, C. K. Lee and A. R. West, High oxide ion conductivity in Bi_2MoO_6 oxidation catalyst, *J. Mater. Chem.*, 2002, **12**, 17–19.
- V. Yu, E. Yanova, R. R. Shafigina, E. S. Buyanova, V. M. Zhukovskii, V. M. Zainullina and S. A. Petrova, Oxide ion conductors of the BIMEVOX Family: synthesis, Structure, and conductivity, *Russ. J. Phys. Chem.*, 2006, **80**, 1725–1730.
- M. J. Godinho, P. R. Bueno, M. O. Orlandi, E. R. Leite and E. Longo, Ionic conductivity of $\text{Bi}_4\text{Ti}_{0.2}\text{V}_{1.8}\text{O}_{10.7}$ polycrystalline ceramics obtained by the polymeric precursor route, *Mater. Lett.*, 2003, **57**, 2540–2544.
- J. A. Collado, M. A. G. Aranda, A. Cabeza, P. Olivera-Pastor and S. Bruque, Synthesis, structure and thermal expansion of the $\text{La}_2\text{W}_{2-x}\text{Mo}_x\text{O}_9$ Series, *J. Solid State Chem.*, 2002, **167**, 80–85.
- X. P. Wang, Q. F. Fang, Z. S. Li, G. G. Zhang and Z. G. Yi, Dielectric Relaxation studies of B-doping effects on the oxygen-ion diffusion in $\text{La}_{2-x}\text{Bi}_x\text{Mo}_2\text{O}_9$ oxide-ion conductors, *Appl. Phys. Lett.*, 2002, **81**, 3434–3436.
- X. P. Wang, Q. F. Fang, Z. S. Li, G. G. Zhang and Z. G. Yi, Dielectric Relaxation studies of B-doping effects on the oxygen-ion diffusion in $\text{La}_{2-x}\text{Bi}_x\text{Mo}_2\text{O}_9$ oxide-ion conductors, *Appl. Phys. Lett.*, 2002, **81**, 3434–3436.
- T. Paul and A. Ghosh, Conduction and Relaxation mechanism in bismuth doped $\text{La}_2\text{Mo}_2\text{O}_9$ ionic conductors, *J. Appl. Phys.*, 2013, **114**, 164101–7.
- F. Goutenoire, O. Isnard, E. Suard, O. Bohnke, Y. Lalignant, R. Retoux and P. Lacorre, *J. Mater. Chem.*, 2001, **11**, 119.
- D. M. Lopez, J. C. Vazquez, W. Zhou, J. T. S. Irvine and P. Nunez, Structural studies on W^{6+} and Nd^{3+} substituted $\text{La}_2\text{Mo}_2\text{O}_9$ materials, *J. Solid State Chem.*, 2006, **179**, 278–288.
- J. Yang, Z. Gu, Z. Wen and D. Yan, Preparation and characterization of solid electrolytes $\text{La}_{2-x}\text{A}_x\text{Mo}_{2-y}\text{W}_y\text{O}_9$ (A = Sm, Bi), *Solid State Ionics*, 2005, **176**, 523–530.
- T. He, Y. Huang, Q. He, Y. Ji, L. Pei, J. Liu and Z. Lu, The effects on the structure and properties in the oxide-ion conductor $\text{La}_2\text{Mo}_2\text{O}_9$ by partial substituting Ba for La, *J. Alloys Compd.*, 2005, **388**(1), 145–152.

- 24 C. Tealdi, G. Chiodelli, L. Malavasi and G. Flor, Effect of alkaline-doping on the properties of $\text{La}_2\text{Mo}_2\text{O}_9$ fast oxygen ion conductor, *J. Mater. Chem.*, 2004, **14**, 3553–3557.
- 25 X. P. Wang and Q. F. Fang, Effect of Ca doping on the oxygen ion diffusion and phase transition in oxide ion conductor $\text{La}_2\text{Mo}_2\text{O}_9$, *Solid State Ionics*, 2002, **146**, 185–193.
- 26 S. George, F. Goutenoire, F. Altorfer, D. Sheptyakov, F. Fauth, E. Suard and P. Lacorre, *Solid State Ionics*, 2003, **161**, 231–241.
- 27 R. Subasri, D. Matusch, H. Nafe and F. Aldinger, Synthesis and characterization of $(\text{La}_{1-x}\text{M}_x)_2\text{Mo}_2\text{O}_{9-\delta}$; $\text{M} = \text{Ca}^{2+}$, Sr^{2+} or Ba^{2+} , *J. Eur. Ceram. Soc.*, 2004, **24**(1), 129–137.
- 28 B. Yan, M. Li and J. Zhang, Structural and electrical properties of $\text{La}_{2-x}\text{Sr}_x\text{Mo}_2\text{O}_9$, *J. Rare Earths*, 2013, **31**(4), 428–433.
- 29 K. S. Yoo and A. J. Jacobson, Effect of Sr and Cr doping on properties of $\text{La}_2\text{Mo}_2\text{O}_9$ electrolytes, *J. Mater. Sci.*, 2005, **40**, 4431–4434.
- 30 J. Yang, Z. Gi, Z. Wen and D. Yan, Preparation and characterization of solid electrolytes $\text{La}_{2-x}\text{A}_x\text{Mo}_{2-y}\text{W}_y\text{O}_9$ ($\text{A} = \text{Sm}$, Bi), *Solid State Ionics*, 2005, **176**, 523–530.
- 31 D. S. Tsai, M. J. Hsieh, J. C. Tseng and H. Y. Lee, Ionic conductivities and phase transitions of lanthanide rare earth substituted $\text{La}_2\text{Mo}_2\text{O}_9$, *J. Eur. Ceram. Soc.*, 2005, **25**(4), 481–487; D. Marrero-Lopez, J. Pena-Martinez, D. Perez-Coll and P. Nunez, Effects of preparation method on the microstructure and transport properties of based materials, *J. Alloys Compd.*, 2006, **422**(1–2), 249–257.
- 32 D. Marrero-Lopez, J. Canales-Vazquez, J. C. Ruiz-Morales, J. T. S. Irvine and P. Nunez, Electrical conductivity and redox stability of $\text{La}_2\text{Mo}_{2-x}\text{W}_x\text{O}_9$ materials, *Electrochim. Acta*, 2005, **50**, 4385–4395.
- 33 G. Corbel, Y. Lalignant, F. Goutenoire, E. Suard and P. Lacorre, Effects of Partial substitution of Mo^{6+} by Cr^{6+} and W^{6+} on crystal structure of the fast oxide-ion conductor structural effects of W^{6+} , *Chem. Mater.*, 2005, **17**, 4678–4684.
- 34 S. Basu and H. S. Maiti, Ion Dynamics study of Nb^{5+} substituted $\text{La}_2\text{Mo}_2\text{O}_9$ by AC impedance spectroscopy, *J. Electrochem. Soc.*, 2009, **156**(7), 114–116.
- 35 D. Li, X. P. Wang, Z. Zhuang, J. X. Wang, C. Li and Q. F. Fang, Reducibility study of oxide-ion conductors $\text{La}_{2-x}\text{Ba}_x\text{Mo}_{2-y}\text{A}_y\text{O}_{9-\delta}$ ($\text{A} = \text{W}$, Al , Ga) assessed by impedance spectroscopy, *Mater. Res. Bull.*, 2009, **44**(2), 446–450.
- 36 C. Li, X. P. Wang, J. X. Wang, D. Li, Z. Zhuang and Q. F. Fang, Study on the electrical conductivity and oxygen diffusion of oxide-ion conductors $\text{La}_2\text{Mo}_{2-x}\text{T}_x\text{O}_{9-\delta}$ ($\text{T} = \text{Al}$, Fe , Mn , Nb , V), *Mater. Res. Bull.*, 2007, **42**(6), 1077–1084.
- 37 R. Subasri, H. Nafe and F. Aldinger, On electronic and ionic transport properties of $\text{La}_2\text{Mo}_2\text{O}_9$, *Mater. Res. Bull.*, 2003, **38**, 1965–1977.
- 38 S. Georges, F. Goutenoire, Y. Lalignant and P. Lacorre, Reducibility of fast oxide-ion conductors $\text{La}_{2-x}\text{R}_x\text{Mo}_{2-y}\text{W}_y\text{O}_9$ ($\text{R} = \text{Nd}$, Gd), *J. Mater. Chem.*, 2003, **13**, 2317–2321.
- 39 L. Haoran, W. Chang-An and M. A. White, Complex effect of $\text{Sm}^{3+}/\text{W}^{6+}$ co-doping on α - β phase transformation and phonon scattering of oxygen deficient $\text{La}_2\text{Mo}_2\text{O}_9$, *J. Am. Ceram. Soc.*, 2015, **98**, 1385–1388.
- 40 L. Malavasi, H. J. Kim, S. J. L. Billinge, T. Proffen, C. Tealdi and G. Flor, Nature of the Monoclinic to Cubic Phase Transition in the Fast Oxygen Ion Conductor $\text{La}_2\text{Mo}_2\text{O}_9$ (LAMO), *J. Am. Chem. Soc.*, 2007, **129**(21), 6903–6907.
- 41 M. Guzik, M. Bieza, E. Tomaszewicz, Y. Guyot, G. Boulon and Z. Naturforsch., Development of Nd^{3+} -doped Monoclinic Dimolybdates $\text{La}_2\text{Mo}_2\text{O}_9$ as Optical Materials, *Z. Naturforsch., B: J. Chem. Sci.*, 2014, **69**, 193–204.
- 42 A. G. Selmi, G. Corbel, S. Kojikian, V. Voronkova, E. Kharitonova and P. Lacorre, Complex effect of partial substitution of La^{3+} by Ca^{2+} on the stability of fast oxide-ion conductor $\text{La}_2\text{Mo}_2\text{O}_9$, *Eur. J. Inorg. Chem.*, 2018, **1**, 1813–1821.
- 43 I. R. Evans, J. A. K. Howard and J. S. O. Evans, The crystal structure of α - $\text{La}_2\text{Mo}_2\text{O}_9$ and structural origin of the oxide ion migration pathway, *Chem. Mater.*, 2005, **17**, 4074–4077.
- 44 N. Mhadhbi, *Doctoral thesis*, University of Maine, Maine, France, 2012.
- 45 T. Paul and A. Ghosh, Structure and vibrational properties of $\text{La}_{2-x}\text{Bi}_x\text{Mo}_2\text{P}_9$ ($0.05 \leq x \leq 0.4$) oxygen ion conductors, *J. Alloys Compd.*, 2014, **613**, 146–152.
- 46 M. Guzik, M. Bieza, E. Tomaszewicz, Y. Guyot and G. Boulon, Development of Nd^{3+} -doped Monoclinic dimolybdates $\text{La}_2\text{Mo}_2\text{O}_9$ as optical materials, *Z. Naturforsch., B: J. Chem. Sci.*, 2014, **69**, 193–204.
- 47 M. Isaac, V. U. Nayar, D. D. Makitova, V. V. Tkachev and L. O. Atovmjan, Infrared and polarized Raman Spectra of $\text{LiNa}_3(\text{MoO}_4)_2 \cdot 6\text{H}_2\text{O}$, *Spectrochim. Acta, Part A*, 1997, **53**, 685–691.
- 48 W. Liu, W. Pan, J. Luo, A. Godfrey, G. Ou, H. Wu and W. Zhang, Stressed phase transition and giant ionic conductivity in $\text{La}_2\text{Mo}_2\text{O}_9$ nanowires, *Nat. Commun.*, 2015, **6**, 8354–8358.
- 49 Q. He, M. Sun, X. J. Kuan, B. Huang, S. Ye and Q. Y. Zhang, Unraveling the correlation between oxide-ion motion and upconversion luminescence in β - $\text{La}_2\text{Mo}_2\text{O}_9:\text{Yb}^{3+}, \text{Er}^{3+}$ derivatives, *J. Mater. Chem. C*, 2017, **5**, 10965–10970.
- 50 K. Karinuma, N. Takahashi, H. Yamamura, K. Nomura and T. Atake, *Solid State Ionics*, 2004, **168**, 69–74.
- 51 K. Nakamoto, *Infrared and Raman Spectra of Inorganic and coordination compounds Part a: theory and Applications in Inorganic Chemistry*, Wiley, NJ, 6th edn, 2009.
- 52 A. A. Porporati, K. Suji, M. Valant and A. K. Axelsson, Raman tensor elements for multiferroic BiFeO_3 with rhombohedral $R3c$ symmetry, *J. Raman Spectrosc.*, 2010, **41**, 84–87.
- 53 S. Chaturvedi, R. Bag, V. Sathe, S. Kulkarni and S. Singh, Holmium induced enhanced functionality at room temperature and structural phase transition at high temperature

- in bismuth ferrite nanoparticles, *J. Mater. Chem. C*, 2016, **4**, 780–792.
- 54 M. Nadeem, W. Khan, S. Khan, S. Husain and A. Ansari, Tailoring dielectric properties and multiferroic behaviour of nanocrystalline BiFeO₃ via Na doping, *J. Appl. Phys.*, 2018, **124**, 164105-9.
- 55 S. Sayyed, S. A. Acharya, P. Kautkar and V. Sathe, Structural and dielectrics anomalies near the MPB region of Na_{0.5}Bi_{0.5}TiO₃-SrTiO₃ solid solution, *RSC Adv.*, 2015, **5**, 50644–50654.
- 56 V. V. Atuchin, A. S. Aleksandrovsky, O. D. Chimitiva, T. A. Gavrilova, A. S. Krylov, M. S. Molokeev, A. S. Oreshonkov, B. G. Bazarov and J. G. Bazarova, Synthesis and spectroscopic properties of Monoclinic α -Eu₂(MoO₄)₃, *J. Phys. Chem. C*, 2014, **118**, 15404–15411.
- 57 A. S. Nowick and B. S. Berry, *Anelastic Relaxation in Crystalline Solids*, Academic, New York, 1972.
- 58 F. P. Wang and Q. F. Fang, Mechanical and dielectric relaxation studies on the mechanism of oxygen ion diffusion in La₂Mo₂O₉, *Phys. Rev. B: Condens. Matter Mater. Phys.*, 2002, **65**, 064304-6.
- 59 C. Ang, Z. Yu and L. E. Cross, Oxygen-vacancy-related low-frequency dielectric relaxation and electrical conduction in Bi:SrTiO₃, *Phys. Rev. B: Condens. Matter Mater. Phys.*, 2000, **62**, 228–234.
- 60 M. Weller and H. Schubert, Internal Friction, Dielectric Loss, and Ionic Conductivity of Tetragonal ZrO₂@3% Y₂O₃(Y@TZP), *J. Am. Ceram. Soc.*, 1986, **69**, 573–577.
- 61 D. Li, X. P. Wang, Q. F. Fang, J. X. Wang, C. Li and Z. Zhuang, Phase transition associated with the variation of oxygen vacancy/ion distribution in the oxide-ion conductor La₂Mo_{2-x}W_xO₉, *Phys. Status Solidi A*, 2007, **204**(7), 2270–2278.
- 62 Q. F. Fang, X. P. Wang, G. G. Zhang and Z. G. Yi, Damping mechanism in the novel La₂Mo₂O₉-based oxide-ion conductors, *J. Alloys Compd.*, 2003, **355**, 177–182.
- 63 Aakansha and S. Ravi, Influence of Cr substitution on magnetic and dielectric properties of gadolinium iron garnets, *Solid State Commun.*, 2019, **300**, 113690.
- 64 R. J. Macdonald, Accurate fitting of immittance spectroscopy frequency-response data using the stretched exponential model, *J. Non-Cryst. Solids*, 1997, **212**, 95–116.
- 65 R. K. Panda and D. Behera, Investigation of electric transport behavior of bulk CoFe₂O₄ by complex impedance spectroscopy, *J. Alloys Compd.*, 2014, **587**, 481–486.
- 66 D. S. Tsai, M. J. Hsieh, J.-C. Tseng and H.-Y. Lee, Ionic conductivities and phase transitions of lanthanide rare-earth substituted La₂Mo₂O₉, *J. Eur. Ceram. Soc.*, 2005, **25**, 481–487.
- 67 T. Y. Jin, M. V. Madhava Rao, C. L. Cheng, D. S. Tsai and M. H. Hung, Structural stability and ion conductivity of the Dy and W substituted La₂Mo₂O₉, *Solid State Ionics*, 2007, **178**, 367–374.
- 68 F. Goutenoire, O. Isnard, E. Suard, O. Bohnke, Y. Laligant, R. Retoux and P. Lacorre, Structural and transport characteristics of the LAMOX family of fastoxide-ion conductors, based on lanthanum molybdenum oxide La₂Mo₂O₉, *J. Mater. Chem.*, 2001, **11**, 119–124.
- 69 V. V. Kharton, F. M. B. Marques and A. Atkinson, Transport properties of solid oxide electrolyte ceramics: a brief review, *Solid State Ionics*, 2004, **174**(1–4), 135–149.
- 70 L. Ge and K. Guo, Sinterability, reducibility, and electrical conductivity of fast oxide-ion conductors La_{1.8}R_{0.2}MoWO₉(R = Pr, Nd, Gd and Y), *Ceram. Int.*, 2015, **41**, 10208–10215.